Advanced Steel Construction – Vol. 18 No. 3 (2022) 670–678
DOI:10.18057/IJASC.2022.18.3.4

LOW-TEMPERATURE COMPRESSION BEHAVIOUR OF CIRCULAR STUB STAINLESS-STEEL TUBULAR COLUMNS

Jia-Bao Yan [1, 2], Biao Zhang [2], Jun-Ying Feng [2], Yan-Sheng Du [1, 2, *], Yun-Biao Luo [1, 2] and Yun-Dong Shi [1, 2]

[1] *Key Laboratory of Coast Civil Structure Safety of Ministry of Education, Tianjin University, Tianjin 300350, China*
[2] *School of Civil Engineering, Tianjin University, Tianjin 300350, China*
** (Corresponding author: E-mail: duys@tju.edu.cn)*

ABSTRACT

This paper firstly studies mechanical properties of stainless steel (SS) S30408 at the low temperature (*T*) range of -80~20℃. Further compression tests are carried out on 20 SS stub tubular columns (SSSTCs) at low temperatures of -80, -60, -30, and 20℃ to investigate their low-temperature compression behaviour. Including the testing low temperatures, the wall thickness of SS tube (*t*) is the other investigated parameters. Test results show that decreasing the *T* from 20 to -80℃ improves the yield and ultimate strength of stainless steel by 29% and 80%, respectively, but reduces its ductility by about 25%. Under low-temperature compression, elephant foot local buckling occurs to most of SSSTCs and inelastic inward and outward local buckling occurred to specimens with 6 mm-thick SS tube. Test results also show that the decreasing *T* value increases the strength and stiffness of SSSTCs, but compromises their ductility; the wall thickness of SSSTCs significantly improves their strength, stiffness, and ductility. This paper also develops 3D finite element model (FEM) to estimate the low-temperature compression behaviour of SSSTCs, which considers nonlinearities of material and geometry, geometric imperfections, and influences of low temperatures. The validations show it predicts reasonably well the low-temperature compression behaviours of SSSTCs.

ARTICLE HISTORY

Received: 26 June 2021
Revised: 16 December 2021
Accepted: 21 December 2021

KEYWORDS

Stainless steel;
Low temperture;
Compression test;
Arctic engineering;
Finite element;
Compression behaviour

1. Introduction

Stainless steel (SS) possesses extensive advantages of high ductility, high environmental corrosion resistance, attracting architectural appearance, low maintenance costing, good processability and weldability, and recycling potentiality. Due to these extensive advantages, stainless steel gains increasing engineering applications especially in applications of infrastructures exposed to environmental pollution and chloride attack, e.g., roofs of buildings, offshore/onshore bridges, and harbour facilities. After its first application in Brearley (UK) and Maurer and Strauss in Germany [1], more representative engineering applications include roofs of Empire State Building and Chrysler Building in USA, Expo MRT station in Singapore, Tokyo Stadium in Japan, Millennium footbridge in UK, foot and road bridge near Siena, Shenzhen Bay bridge. Three representative types of SS are austenitic, duplex and ferritic SS [3]. Austenitic S30408 SS, a type of commonly used austenitic stainless steel, has been used in architectures, bridges, oil and chemical industry buildings, LNG containers, and pressure vessels [4-7] More recently, it has been proposed for the coastal bridges in cold regions (see Fig. 1).

The low temperature (*T*) in cold regions varies, e.g., the lowest recorded *T* in Northern China is about -50℃, the recorded lowest *T* in the Arctic and Antarctic varies from -68.0 to -89.2℃ [8]. Thus, these low temperatures tend to affect the structural behaviours of Austenitic S30408 SS used in cold-region constructions. Extensive previous studies on SS have been performed on their ambient/high-temperature structural performances. Rasmussen [9], Ashraf et al. [10], and Gardener and Netehrcot [11] contributed to mechanical properties (MPs) of SS at ambient temperatures. Quach et al. [12] and Gardner and Yun [13] proposed stress-strain constitutive models for SS. Extensive experimental and analytical works on MPs of SS at high temperatures have also extensively reported by Sakumot et al. [14], Chen and Young [15], Gardner et al. [16], Wang et al. [17], Liang et al. [18], and Fan et al. [19-20]. Rasmussen [21] studied the structural behaviours of SS tubular structures. Young and Hartono [22] investigated compression behaviours of SS tubes at room temperatures. Lui et al. [23] experimentally studied ultimate strength behaviours of SS beam-columns. Huang and Young [24] and Arrayago et al. [25] also contributed to the topic of SS beam-columns. Bu and Gardner [26] studied the structural behaviours of laser-welded SS beam-columns. Greiner and Kettler [27] studied the bending-compression interaction behaviour of SS members. Zhao et al. [28] contributed to the bending-compression interaction behaviour of slender SS members. Cai and Young [29] studied the structural behaviour of cold-formed stainless steel bolted connections at post-fire condition. Salih et al. [30] numerically studied the net section failure behaviours of SS bolted connections. Elflah [31] studied the behaviour of SS beam-column joints. Though these extensive studies made solid pavements on the applications of SS structures, they mainly concentrated on the material/member behaviours of SS at ambient/high temperatures. The information on SS materials or members is still very limited. Studies on the SS structural members at low temperatures become necessary to promote their applications.

This paper studied the compression behaviour of stub SS tubular columns (SSSTCs) at low temperatures. Twenty SSSTCs with varying wall thickness (*t*) were tested at four *T* levels of -80, -60, -30, and 30℃. Test results provided useful information on the compression behaviours of SSSTCs at low temperatures. The effects of *T* and *t* were detailed analysed and discussed. Moreover, this paper developed finite element models (FEMs) to estimate the low-temperature compression behaviour of SSSTCs, and these FEMs were validated by the reported 20 tests. At the end of this paper, conclusions were given based on these experimental and numerical investigations.

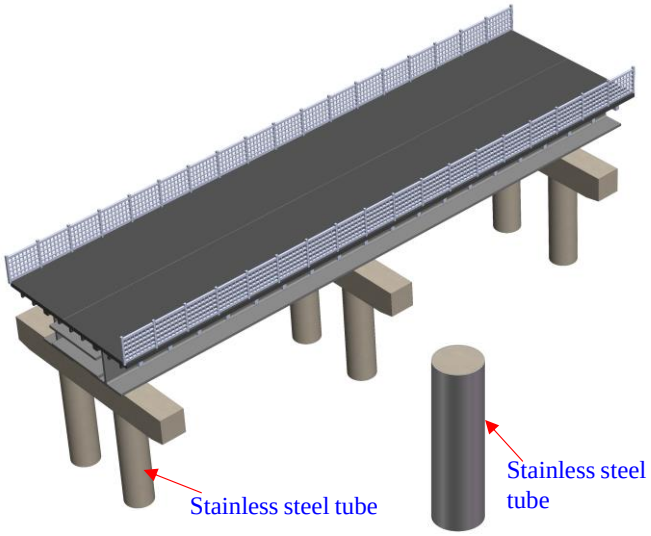

Fig. 1 Applications of stainless steel tubular columns in a composite bridge

2. Axial compression tests on stub stainless steel tubular columns (SSSTCs)

2.1. Testing program

Stainless steel S30408 was adopted to fabricate the SSSTCs. Table 1 lists the chemical compositions of S30408 and compared with those of mild steel Q345 with the close strength. It can be found that the SS S304 contains much

higher Chromium (Cr) (18.24%) and Nickel (Ni) (8.02%) than mild steel Q345, which are the main reason of high corrosion resistance of S304. To study the axial low-temperature compression behaviour of SSSTCs, 20 SSSTCs using S304 SS were prepared with three types of wall thickness (t), i.e., *t*=3.0, 4.5,

Table 1
Chemical composition of mild steel Q345 and stainless steel S30408

Chemical composition	C (%)	Si (%)	Mn (%)	S (%)	P (%)	Cr (%)	Ni (%)
Q345	0.14	0.55	1.40	-	-	0.30	0.30
S30408-3mm	0.043	0.50	1.51	0.002	0.035	18.24	8.01
S30408-4mm	0.043	0.48	1.45	0.002	0.035	18.27	8.02
S30408-6mm	0.041	0.44	1.27	0.001	0.016	18.47	8.15
	N (%)	Nb (%)	Mo (%)	Cu (%)	Al_s (%)	Ti (%)	V (%)
Q345	0.008	0.021	-	0.30	0.035	0.008	0.03
S30408-3mm	-	-	-	-	-	-	-
S30408-4mm	-	-	-	-	-	-	-
S30408-6mm	0.027	-	-	-	-	-	-

and 6.0 mm. Therefore, these 20 SSSTCs were categorized into three groups with their different *t* values. For each group of SSSTCs with different *t* value, four testing low temperatures were set, i.e., *T*=30, -30, -60, and -80°C. And one/two SSSTCs were prepared for each *T* level. Fig. 2 plots the geometry of SSSTCs. Each SSSTC is 400 mm high with an equal external diameter of 133 mm. Table 1 provides more information on the details of tested SSSTCs.

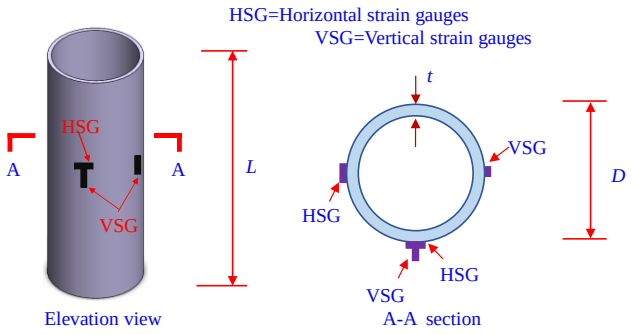

Fig. 2 Diemension of the SSSTCs

Mechanical properties of SS S30408 were obtained from tension tests on coupons cut from those SSSTCs according to GB/T 13239-2006 [32] (See Fig. 3). Tensile stress-strain curves of SS S30408 coupons at different *T* levels are illustrated in Fig. 3(a)-(c). These figures reveal interesting findings as the following:

(1) The mechanical properties of SS are significantly influenced by the reducing *T*. Reducing *T* of the environment improves the yield and ultimate strength, but reduces the ductility of SS. As the *T* decreases from 20 to -30, -60,

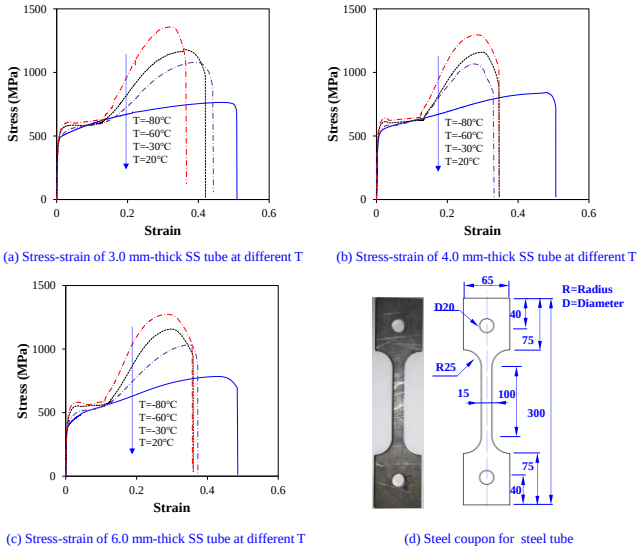

Fig. 3 Low-tempreature tenisle stress-strain curves of SS at different low temperatures

and -80°C, the yield (or ultimate) strength of 3 mm-thick SS coupon is increased by 3% (42%), 6% (58%), and 14% (77%), respectively; the yield (or ultimate) strength of 4.5 mm-thick SS coupon is increased by 6% (27%), 11% (38%), and 24% (54%), respectively; and these increments for 6.0-thick SS coupon equal to 2% (42%), 9% (45%), and 16% (62%), respectively. However, with the decrease of *T* from 20 to -30, -60, and -80°C, the fracture strain of 3 (or 4.5, 6.0) mm-thick SS was reduced by 13% (35%, 19%), 17% (35%, 26%), and 28% (32%, 26%), respectively.

(2) The low-temperature stress-strain curves of SS behave differently from those ambient curves especially at the strain hardening stage. The ambient-temperature stress-strain curves exhibit a flat increasing rate at the strain hardening stage, but the stress-strain curves of SS at low temperatures exhibit much larger increasing slope at the strain hardening branch than that at ambient temperature.

Table 1 provides detailed information on mechanical properties of S30408 at low temperatures.

2.2. Setup and instrumentation

The low-temperature compression tests on SSSTCs were performed by a 300-ton testing machine in Structural Lab of Tianjin University. Fig. 4 shows the setup of compression tests on SSSTCs. Each SSSTC was directly installed to the bottom supporting rigid plate, and surrounded by a cooling chamber made of insulation materials, which was fabricated for simulation on the cold-region environment. LNG was introduced inside the cooling chamber to cool down the SSSTC. PT100 type of thermal couples were also installed on the external surface of SSSTCs at different positions to instrument the low temperatures of SSSTCs as shown in Fig. 4. Furthermore, these monitored temperatures of SSSTCs were used as the referencing temperature readings to control the flow of the injected LNG into the cooling chamber by a magnetic valve (see Fig. 4).

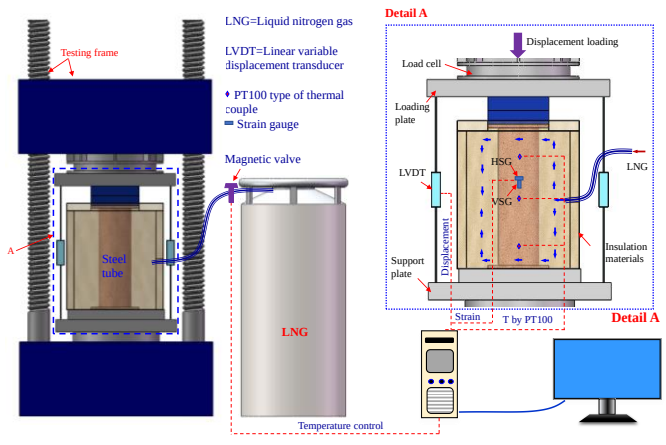

Fig. 4 Setup and instrumentations of low-temperature compression tests on SSSTCs

Displacement loading transferred from the actuator directly acted on the top of SSSTCs, and the reaction forces of the SSSTCs were measured automatically by the testing machine. Shortenings of the SSSTC (Δ) were measured by four

LVDTs installed between the loading and supporting plate (see Fig. 4). The vertical SSSTCs, and the reaction forces of the SSSTCs were measured automatically by the testing machine. Shortenings of the SSSTC (Δ) were measured by four LVDTs installed between the loading and supporting plate (see Fig. 4). The vertical and circumferential strains at the mid-height of SSSTCs were instrumented by linear strain gauges (see Fig. 4), and these measured positions of the SS tube at the locations are shown in Fig. 2.

The geometric imperfections [33] were also measured at different locations of the SS tube prior to the low-temperature compression tests. Fig. 5 plots the measured geometric imperfections at quarter circumferential positions along the height of representative SSSTCs Ct6T-60-1 and Ct6T-80. The maximum measured magnitudes of imperfections for SSSTCs are given in Table 2.

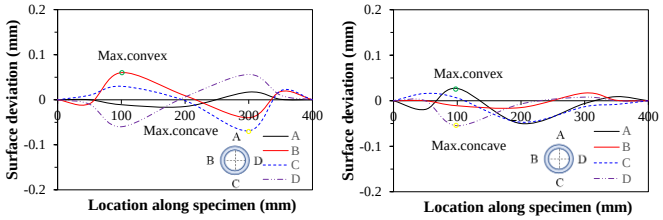

Fig. 5 Measured local geometric imperfections along the height of SSSTCs

Table 2
Details of SSSTCs under low-temperature compression tests

No.	Item	D (mm)	t (mm)	v_0 (mm)	A_s (mm^2)	T (°C)	E_{sT} (GPa)	f_{yT} (MPa)	f_{uT} (MPa)	ε_{yT} (%)	ε_{uT} (%)	ε_{FT} (%)
1	Ct3T20-1	133.1	2.98	0.120	1218	20	170	430	763	0.39	46.91	50.9
2	Ct3T20-2	133.0	3.01	0.130	1229	20	170	430	763	0.39	46.91	50.9
3	Ct3T30	133.1	3.03	0.094	1238	-30	189	442	1080	0.48	39.34	44.3
4	Ct3T60-1	132.8	2.98	0.121	1215	-60	187	456	1209	0.44	35.95	42.0
5	Ct3T60-2	133.1	2.99	0.111	1222	-60	187	456	1209	0.44	35.95	42.0
6	Ct3T80	133.3	3.01	0.120	1231	-80	211	492	1354	0;46	32.03	36.6
7	Ct4.5T20-1	133.2	4.51	0.134	1822	-20	189	434	842	0.40	47.95	50.8
8	Ct4.5T20-2	133.3	4.49	0.108	1816	-20	189	434	842	0.40	47.95	50.8
9	Ct4.5T30-1	133.1	4.49	0.116	1813	-30	224	460	1066	0.40	27.30	33.2
10	Ct4.5T30-2	133.0	4.60	0.100	1855	-30	224	460	1066	0.40	27.30	33.2
11	Ct4.5T60-1	133.1	4.51	0.100	1821	-60	199	481	1158	0.45	29.44	34.7
12	Ct4.5T60-2	133.4	4.50	0.120	1821	-60	199	481	1158	0.45	29.44	34.7
13	Ct4.5T80-1	133.1	4.48	0.092	1809	-80	247	536	1295	0.39	28.08	34.7
14	Ct4.5T80-2	132.9	4.49	0.112	1810	-80	247	536	1295	0.39	28.08	34.7
15	Ct6T20-1	133.1	5.99	0.067	2391	20	173	359	784	0.37	42.41	48.6
16	Ct6T20-2	133.2	6.00	0.100	2396	20	173	359	784	0.37	42.41	48.6
17	Ct6T30	133.3	6.02	0.120	2406	-30	210	367	1116	0.42	32.86	39.5
18	Ct6T60-1	133.0	6.01	0.060	2396	-60	234	393	1139	0.34	29.85	36.0
19	Ct6T60-2	133.1	6.00	0.042	2395	-60	234	393	1139	0.34	29.85	36.0
20	Ct6T80	132.8	6.01	0.027	2393	-80	235	418	1273	0.40	28.70	35.8

D is diameter of circular tube; t denotes thickness of stainless steel tube; v_0 is the initial imperfection amplitude of stainless steel tube by measured; T is low temperature; A_s denotes cross-sectional area of stainless steel tube; f_{yT}, f_{uT}, and E_{sT} denotes yield strength, ultimate strength, and elastic modulus of stainless steel tube, respectively; ε_{yT}, ε_{uT}, and ε_{FT} denotes yield strain, ultimate strain, and fraction strain of stainless steel tube at temperature T.

3. Test result and discussions

3.1. Failure modes

Fig. 6 depicts failure modes of SSSTCs after the compression tests. It shows that most of the SSSTCs exhibit ring-shaped bulge at one or two ends of SSSTCs, namely elephant foot local buckling. This prevalent type of failure mode commonly took place in tubular columns under compression [34-36], which have low imperfections. For several specimens with t=6 mm tested at -30~-80°C, inelastic inward and outward local buckling occurred as shown in Fig. 6.

3.2. Low-temperature compression load-shortening (P-Δ) curves and load-strain (P-strain) curves of SSSTCs

Figs. 7 and 8 plot the P-Δ curves and P-strain curves of SSSTCs subjected to compression at low temperatures, respectively. These curves reflect that all the P-Δ curves behave closely even with some differences in the strength hardening branches, which can be categorized into three types as summarized in Fig. 9. The P-Δ curves of SSSTCs subjected to compression at low temperatures consist of four working stages, namely elastic, inelastic, plastic hardening, and recession stage. The elastic stage initiates from the start of testing and ends at about 50% ultimate load capacity (P_u), which corresponds to the elastic limit of SS stress-strain curves (see Fig. 3). In the following inelastic stage, both P-Δ and P-strain curves exhibit a parabolic manner, which can be also supported by the parabolic stress-strain curves of SS (see Fig. 3). Finally, vertical strains of SSSTCs achieve the yielding value (see Fig. 8). After that, the P-Δ curves enter into their third stage, i.e., plastic stage due to the strain hardening of SS as shown in Fig. 3. The length of the third-stage branch of P-Δ curves was determined by the wall thickness of SSSTCs, which determines the occurrence of local buckling in SS tube. At the third-stage end, the SSSTCs achieve their ultimate capacity (P_u), and local buckling of SSSTCs took place. Finally, the P-Δ curves enter their recession stages. Fig. 8 further confirmed that the measured strains at P_u for all the SSSTCs are beyond yielding point, which implies occurrence of plastic local buckling. In addition, the overturning P-strain curves in Fig. 8 also confirmed the local buckling of SSSTCs.

Fig. 10 plots the representative P/P_u versus hoop-to-vertical strain ($\varepsilon_h/\varepsilon_v$) curves of SSSTCs at low temperatures. It shows that as the P/P_u ratio is below 0.7-0.9, the $\varepsilon_h/\varepsilon_v$ ratio exhibits values near 0.3 (within a range between 0.2 and 0.4), which implies a linear behaviour of the SSSTCs. A_s the P/P_u ratio is beyond 0.9, the $\varepsilon_h/\varepsilon_v$ ratio increases faster that corresponds the nonlinear behaviour of SSSTCs.

3.3. Ultimate load capacity (P_u) and its corresponding shortening (Δ_u), initial stiffness(K_0), and ductility ratio (DI)

Determinations of P_u, Δ_u, K_0, and DI ratio follow the same methods used in Ref. [37]. The K_0 and P_u are determined from the stage I and III branches of P-Δ curves as shown in Fig. 9, which specifies the K_0= $P_{45\%}/\Delta_{45\%}$ ($P_{45\%}$=45%P_u, and $\Delta_{45\%}$ is the shortening at $P_{45\%}$). The Δ_u and DI ratio of SSSTCs are used as the index to reflect the ductility of SSSTCs under compression whilst the DI ratio can be determined by following equation;

$$DI = \frac{\Delta_{85\%}}{\Delta_u} \quad (2)$$

where, $\Delta_{85\%}$ is the shortening at 85%P_u of stage IV branches of P-Δ curves in Fig. 9; Δ_u is the shortening at P_u.

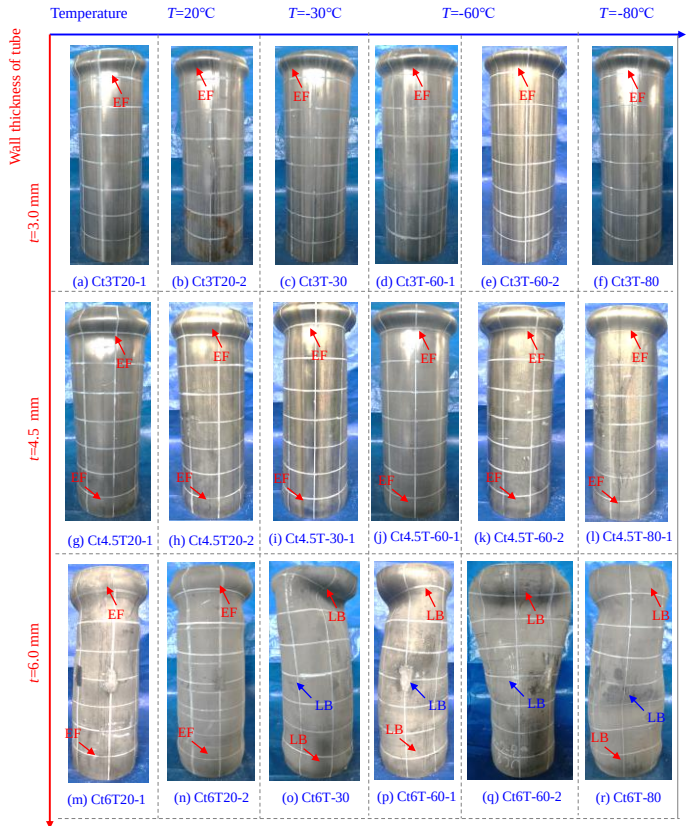

Fig. 6 Failure modes of SSSTCs under low-temperature compression (EF=elephant foot; LB=Local buckling)

Finally, these determined P_u, Δ_u, K_0, and DI ratio are tabulated in Table 3.

3.4. Discussions

3.4.1 Effect of the low temperature (T)

Fig. 11 illustrates the effect of T on low-temperatures compression P-Δ behaviour of SSSTCs. Fig. 12 gives the detailed effects of T on P_u, K_0, Δ_u, and DI ratio of SSSTCs. They show that the decreasing T significantly affected the low-temperature compression behaviour of SSSTCs in terms of improved ultimate load capacity and initial stiffness, and reduced ductility. As reflected in Fig. 12, with the decreases of T from 20 to -30, -60, and -80°C, the average increments in Pu of SSSTCs with wall thickness of 3 mm are 14%, 16%, and 19%, respectively; the average increments in P_u of SSSTCs with wall thickness of 4.5 mm are 2%, 11%, and 13%, respectively; average increments in P_u of SSSTCs with wall thickness of 6.0 mm are 10%, 15%, and 23%, respectively; the K_0 of SSSTCs with 3 (4.5, or 6.0) mm-thick SS tube was averagely increased by 4% (6%, 6%), 5% (15%, 11%), and 8% (25%, 20%), respectively. These findings show that the decreasing T increases both P_u and K_0 of SSSTCs due to the enhancements of both modulus and strength of SS materials by decreasing low temperatures (see Fig. 3). Moreover, the test results also pointed out that with the same decreasing magnitude of T, the SSSTCs with 4.5 and 6.0 mm thick SS tube exhibit much larger improvements on K_0 than that with 3 mm thick SS tube, but the increments of P_u are very close disregarding the thickness of SS tube. This is due to that the decreasing T improves the E_s and strength of SS tube, which explains these improvements on both P_u and K_0. However, the early premature local buckling terminates the fully utilization of these improved ultimate strengths of SS material due to low temperatures, which explains close improvements on P_u of SSSTCs.

However, Fig. 12(c) points out that the decreasing temperature generally decreases the Δ_u of SSSTCs. It shows that with the decreasing T from 20 to -30, -60, and -80°C, the Δ_u of SSSTCs with 3 (4.5, or 6.0) mm-thick SS tube was averagely reduced by 17% (19%, 12%), 15% (23%, 17%), and 16% (21%, -9%), respectively. This is because that the decreasing T improves the strength of SS tube, which reduced its buckling strain compared with that at ambient temperature. Meanwhile, the influences of T on DI ratios of SSSTCs with 3 (4.5, or 6.0) mm-thick SS tube exhibit positive/negative improvements, which might be due to the imperfections and eccentricity of SSSTCs.

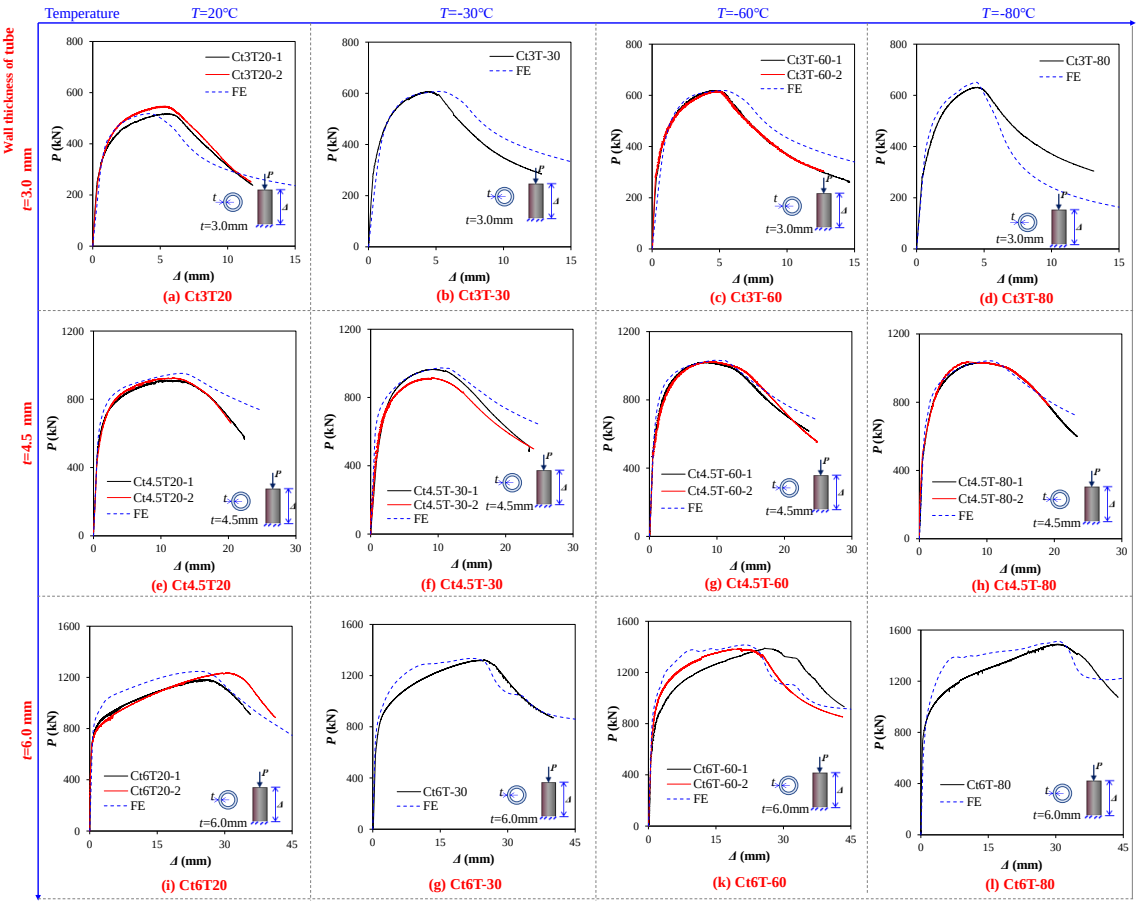

Fig. 7 Load-shortening curves of SSSTCs under low-temperature compression

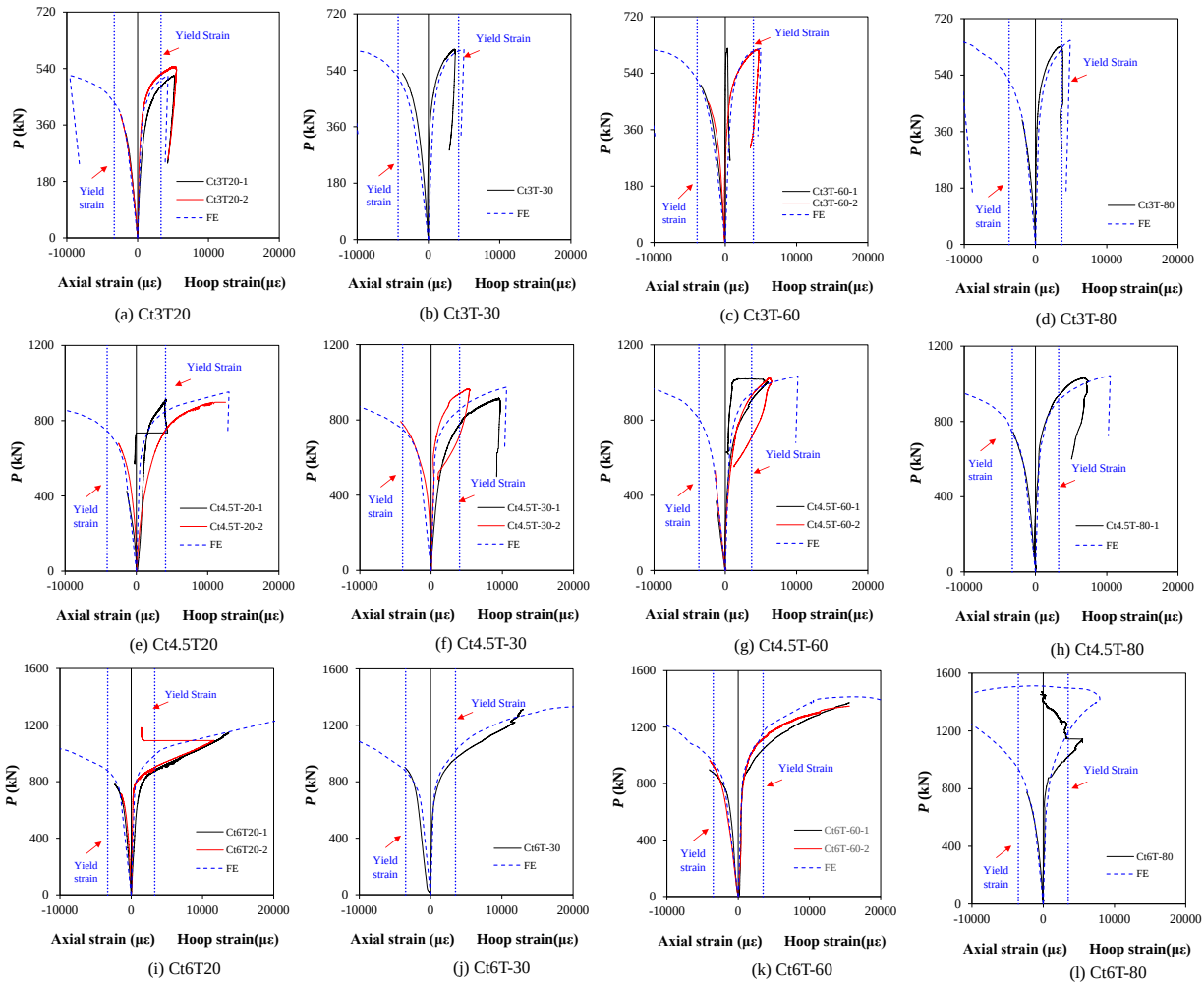

Fig. 8 Load-strain curves of SSSTCs under low-temperature compression (Negative strain denotes compression strain and positive strain denotes tension)

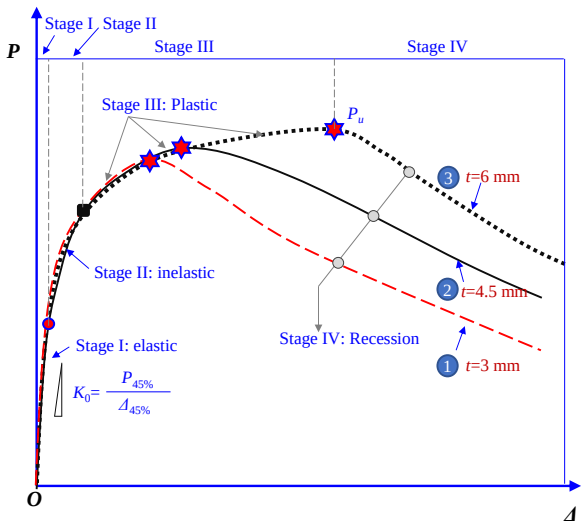

Fig. 9 Generalized *P-Δ* curves of SSSTCs subjected to low-temperature compression

3.4.2 Effect of the thickness of SS tube (t)

Fig. 13 depicts the effect of t on compression *P-Δ* behaviour of SSSTCs. Fig. 14 shows the detailed effects of t on P_u, K_0, Δ_u, and *DI* ratio of SSSTCs. They illustrate that the increasing t of SS tube generally improves both strength and ductility of SSSTCs. As t increases from 3.0 to 4.5 and 6 mm, the P_u values of SSSTCs tested at 20°C (or -30, -60, -80°C) were increased by 73% (65%, 55%, 64%) and 127% (125%, 118%, and 136%), respectively; the K_0 values of SSSTCs tested at 20°C (or -30, -60, -80°C) were increased by 70% (81%, 74%, 70%) and 140% (147%, 144%, and 129%), respectively; the Δ_u values of SSSTCs tested at 20°C (or -30, -60, -80°C) were increased by 110% (91%, 106%, 97%) and 418% (402%, 453%, and 574%), respectively. However, the influences of the increasing t on the *DI* ratio exhibit no obvious improvements as reflected in Fig. 14(d). These increased P_u and K_0 values are due to the enlarged area of cross section and the reduced D/t ratio of SS tube. Meanwhile, the increased Δ_u is mainly due to the reduced D/t ratio from 41 to 30 and 22 as the t increases from 3.0 to 4.5 and 6 mm, respectively.

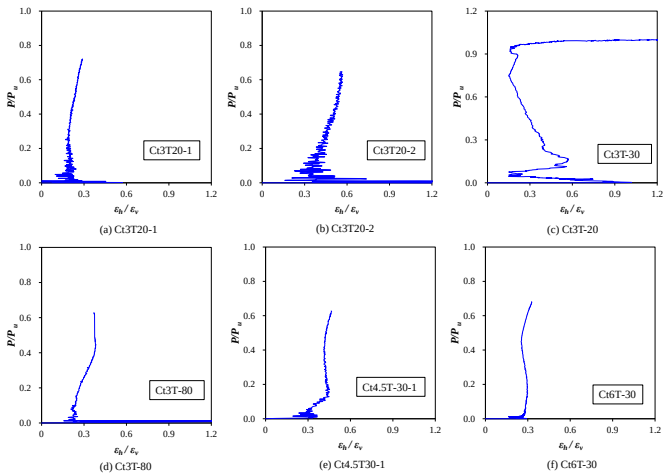

Fig. 10 Generalized P/P_u versus hoop-to-vertical strain curves of SSSTCs at low temperatures

Table 3
Experimental and numerical results of SSSTCs

No.	Item	P_u (kN)	$P_{u,FE}$ (kN)	$P_u/P_{u,FE}$	Δ_u (mm)	$\Delta_{u,FE}$ (mm)	$\Delta_u/\Delta_{u,FE}$	K_0 (kN/mm)	$K_{0,FE}$ (kN/mm)	$K_0/K_{0,FE}$	*DI*
1	Ct3T20-1	517	517	1.00	5.48	4.25	1.29	492	514	0.96	1.36
2	Ct3T20-2	547	517	1.06	5.33	4.25	1.25	480	514	0.93	1.38
3	Ct3T30	607	607	1.00	4.48	5.28	0.85	506	493	1.03	1.40
4	Ct3T60-1	616	619	1.00	4.50	5.28	0.85	514	503	1.02	1.48
5	Ct3T60-2	619	619	1.00	4.71	5.28	0.89	534	503	1.06	1.42
6	Ct3T80	631	650	0.97	4.54	4.50	1.01	610	610	1.00	1.27
7	Ct4.5T20-1	911	952	0.96	10.96	12.97	0.85	836	878	0.95	1.67
8	Ct4.5T20-2	925	952	0.97	11.78	12.97	0.91	819	878	0.93	1.52
9	Ct4.5T30-1	916	973	0.94	9.43	10.60	0.89	881	883	1.00	1.63
10	Ct4.5T30-2	964	973	0.99	9.05	10.60	0.85	878	883	0.99	1.64
11	Ct4.5T60-1	1020	1032	0.99	8.51	10.17	0.84	978	882	1.11	1.84
12	Ct4.5T60-2	1023	1032	0.99	9.07	10.17	0.89	922	882	1.05	1.85
13	Ct4.5T80-1	1032	1042	0.99	8.96	10.17	0.88	1000	890	1.12	1.90
14	C4.5T80-2	1036	1042	0.99	8.96	10.17	0.88	1069	890	1.20	1.90
15	Ct6T20-1	1183	1246	0.95	25.84	24.20	1.07	1175	1174	1.00	1.29
16	Ct6T20-2	1236	1246	0.99	30.19	24.20	1.25	1160	1174	0.99	1.24
17	Ct6T30	1324	1334	0.99	24.76	21.60	1.15	1235	1235	1.00	1.24
18	Ct6T60-1	1388	1415	0.98	25.75	21.70	1.19	1300	1038	1.25	1.42
19	Ct6T60-2	1384	1415	0.98	20.51	21.70	0.95	1288	1038	1.24	1.38
20	Ct6T80	1489	1512	0.99	30.60	30.72	1.00	1398	1174	1.19	1.27
Mean				0.99			0.99			1.05	
Cov				0.02			0.16			0.10	

P_u denotes experimental ultimate compressive resistance of the column; $P_{u,FE}$ denotes ultimate compressive resistance of stainless steel column finite element model; K_0 denotes experimental initial stiffness of steel tube; $K_{0,FE}$ denotes initial stiffness of stainless steel stub tubular column finite element model; Δ_u denotes shortening of the stainless steel tube at P_u; $\Delta_{u,FE}$ denotes shortening of the stainless steel tube at $P_{u,FE}$ of stainless steel stub tubular column finite element model; *DI* is the ductility ratio for the stainless steel tube.

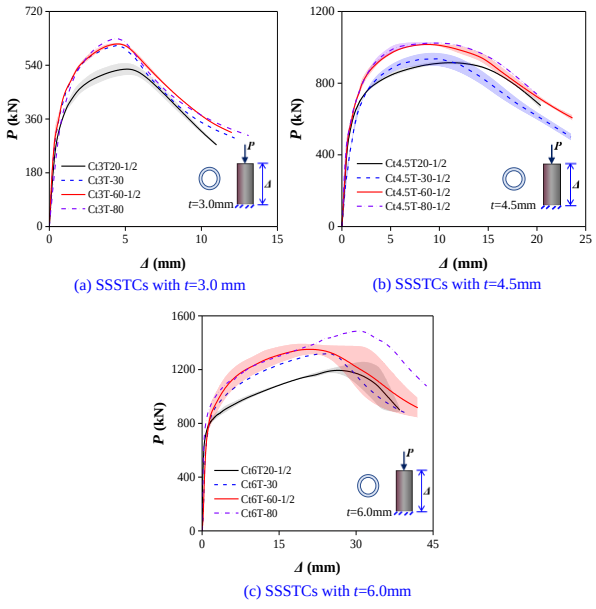

Fig. 11 Effect of *T* on *P*-Δ curves of SSSTCs

and 418% (402%, 453%, and 574%), respectively. However, the influ-

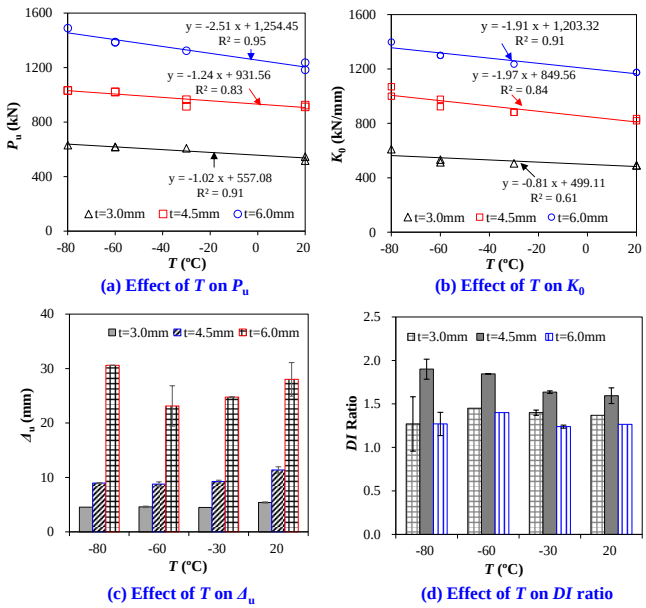

Fig. 12 Effect of *T* on P_u, K_0, and *DI* ratio of SSSTCs

3.4.3. Effect of the thickness of SS tube (t)

Fig. 13 depicts the effect of t on compression *P*-Δ behaviour of SSSTCs. Fig. 14 shows the detailed effects of t on P_u, K_0, Δ_u, and *DI* ratio of SSSTCs.They illustrate that the increasing *t* of SS tube generally improves both strength and ductility of SSSTCs. As *t* increases from 3.0 to 4.5 and 6 mm, the P_u values of SSSTCs tested at 20°C (or -30, -60, -80°C) were increased by 73% (65%, 55%, 64%) and 127% (125%, 118%, and 136%), respectively; the K_0 values of SSSTCs tested at 20°C (or -30, -60, -80°C) were increased by 70% (81%, 74%, 70%) and 140% (147%, 144%, and 129%), respectively; the Δ_u (91%, 106%, 97%)

-ence of the increasing *t* on the *DI* ratio exhibit no obvious improvements as reflected in Fig. 14(d). These increased P_u and K_0 values are due to the enlarged area of cross section and the reduced *D*/*t* ratio of SS tube. Meanwhile, the increased Δ_u is mainly due to the reduced *D*/*t* ratio from 41 to 30 and 22 as the *t* increases from 3.0 to 4.5 and 6 mm, respectively. (91%, 106%, 97%) and 418% (402%, 453%, and 574%), respectively. However, the influences of the increasing *t* on the *DI* ratio exhibit no obvious improvements as reflected in Fig. 14(d). These increased P_u and K_0 values are due to the enlarged area of cross

section and the reduced *D/t* ratio of SS tube. Meanwhile, the increased Δ_u is mainly due to the reduced *D/t* ratio from 41 to 30 and 22 as the *t* increases from 3.0 to 4.5 and 6 mm, respectively.

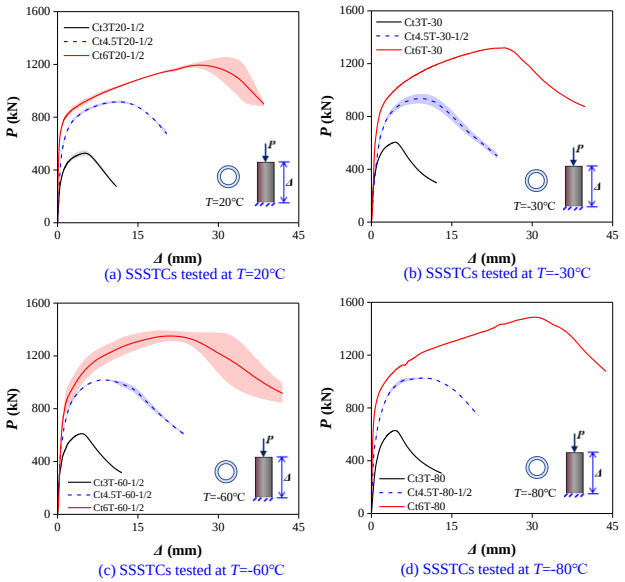

(a) SSSTCs tested at *T*=20°C (b) SSSTCs tested at *T*=-30°C

(c) SSSTCs tested at *T*=-60°C (d) SSSTCs tested at *T*=-80°C

Fig. 13 Effect of *t* on *P-Δ* curves of SSSTCs

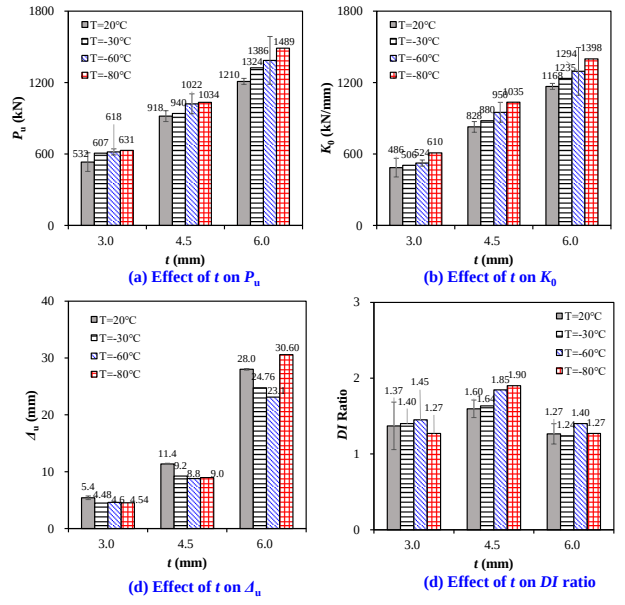

Fig. 14 Effect of *t* on P_u, K_0, and *DI* ratio of SSSTCs

4. Finite element analysis on low-temperature axial compression behaviour of SSSTCs

4.1. General

The developments of finite element model (FEM) on compression behaviour of SSSTCs at low temperatures adopted the general finite element software.SSSTCs at low temperatures adopted the general finite element software. ABAQUS 6.14 [38]. ABAQUS/CAE and ABAQUS/Standard implicit solver were adopted for the modelling and solution, respectively.

4.2. Modelling of SS materials

The typical elastic-plastic model was adopted for the simulation of SS material. This model with kinematic hardening defined the isotropic yielding surface following the von-Mises rule. In ABAQUS, the elastic and plastic behaviours were required to be defined for the isotropic model. In the elastic behaviour, the elastic modulus and Poisson's ratio of SS at low temperatures were required to be input, which can be obtained from test values as reported in Fig. 3. For the plastic behaviour, the true stress versus inelastic strain at low temperatures were required as the input information. The true stress versus inelastic strain of SS are obtained from those engineering stress-strain curves (see Fig. 3) using the following formulae;

$$\varepsilon_{\text{true}} = \ln(1+\varepsilon_{\text{nom}}) \tag{2}$$

$$\sigma_{\text{ture}}^{\text{pl}} = \ln(1+\sigma_{\text{nom}}) - \frac{\sigma_{\text{true}}}{E_{\text{sT}}} \tag{3}$$

where, σ_{ture} and $\varepsilon^{pl}_{\text{ture}}$ denote the true stress and inelastic true strain, respectively; σ_{nom} denotes engineering stress; ε_{nom} denotes engineering strain; E_{sT} is the modulus at *T*.

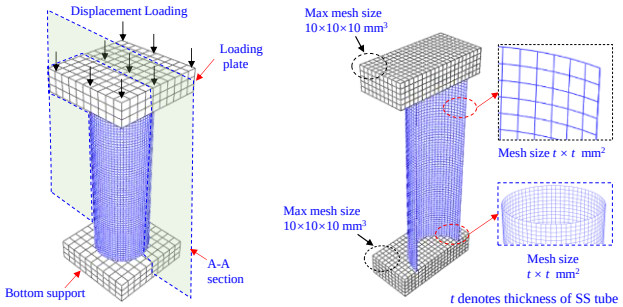

(a) 3D FEM (b) Cross section A-A

Fig. 15 Finite element model for SSSTCs at low temperatures

4.3. Detials of FEM

Fig. 15 shows the built FEM for SSSTCs at low temperatures, which consists of a bottom support plate, a top loading plate, and a SS tube. 3D eight-node continuum element with reduced integration points (C3D8R) was selected for the modelling of top and bottom plate. Four-node doubly-curved shell element (S4R) with reduced integration point and enhanced hourglass control was selected for SS tube [39], which accounts the finite membrane strains and allows transverse shear deformation [38]. A general mesh size of 10×10×10 mm^3 was used for the modelling of both top and bottom plates. Since different mesh sizes of the S4R for the SS tube affect the FE simulation, their influences have also been investigated. Uniform mesh sizes in the vertical and circumferential directions were used in the FEM. Three kinds of mesh size namely type A~C equalling to 0.5*t*×0.5*t*, *t*×*t*, and 2*t*×2*t* mm^2, respectively, were used in the FEM as shown in Fig. 16(a)-(c). Fig. 16(d)-(e) illustrates the influences of different mesh sizes on the FEM simulation results. It shows that as the mesh size decreases the FEM simulated *P-Δ* curves tend to converge to the experimental curves, which implies that the FEM with type A and B mesh sizes of S4R elements offer more accurate simulation results than that with type C mesh size. However, the differences of *P-Δ* curves between FEM with type A and B mesh size are quite limited. Thus, considering the balance of FEM simulation accuracy and efficiency, type B mesh size is finally chosen for the FE modelling.

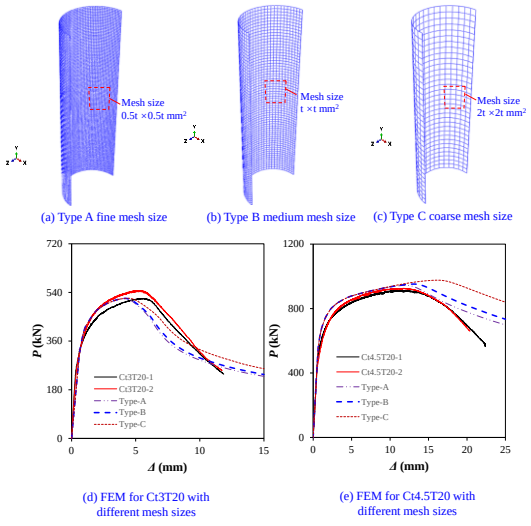

(a) Type A fine mesh size (b) Type B medium mesh size (c) Type C coarse mesh size

(d) FEM for Ct3T20 with different mesh sizes (e) FEM for Ct4.5T20 with different mesh sizes

Fig. 16 Influences of different mesh size on the FEM simulation results

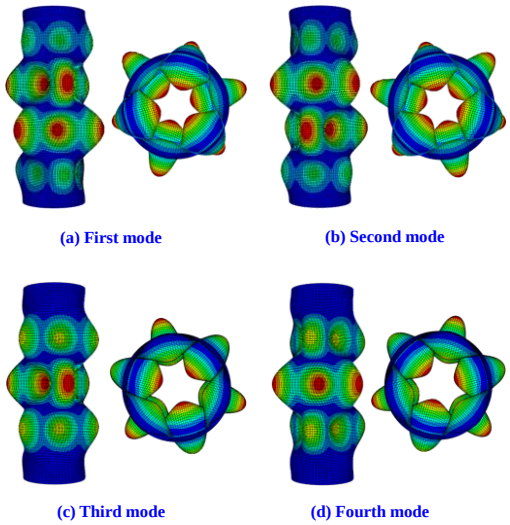

Fig. 17 First four local buckling mode of SSSTCs

4.4. Boundary conditions and geometric imperfections

For each SSSTC, contact algorithm was used to simulate the interactions between two end plates and the SSSTC. "Hard contact", an algorithm defining transfer of pressure between two contacting surfaces and no pressure transferred once those two contacting surfaces are separated, was used to define the interactions perpendicular to the interacting surface between the bottom/loadingend plate and SSSTCs. "Penalty friction" algorithm, adopting a friction coefficient of 0.3, was used for the simulation of interactions along the interacting surfaces between the bottom/loading end plate and SSSTCs. The bottom end plate was restrained from moving whilst the displacement loading was applied on the top plate. A loading eccentricity of $L/2000$ [40] was also used in the FEM to considering its influence on the simulation (L is the height of SSSTC).

Initial geometric imperfection of SSSTCs is mainly produced in the fabrication process of the SS tube, which could affect the developments of local buckling, plastic-initiation load, ultimate load, and post-peak response of SSSTCs at low temperatures. Thus, it requires to consider the geometric imperfections in the FEM. To realize the geometric imperfection of SSSTCs, the local-buckling mode analysis was firstly performed as shown in Fig. 17. Finally, the first buckling mode was chosen, and the magnitude is chosen as the measured magnitude for each specimen as listed in Table 2.

4.5. Validations

The FEM simulated P-Δ and load-strain curves of 20 SSSTCs are compared with those experimental curves in Fig. 7 and 8, respectively. They illustrate that the developed FEM predicted reasonably well load versus shortening/strain behaviours of SSSTCs suffering low-temperature compression. Table 3 lists FE predictions of K_0, P_u, and Δ_u as well as those corresponding test values, and Fig. 19 provides scatters of the prediction-to-test ratios of K_0, P_u, and Δ_u. From these comparisons, it reveals that the developed FEM offers average test-to-FE prediction ratios (or Cov) of 0.99 (0.02), 0.99 (0.16), and 1.05 (0.10) for P_u, Δ_u and K_0, respectively. These discrepancies of FE simulations are probably due to (1) insufficient estimation on the geometric imperfections, (2) inaccurate estimations on the eccentricity of SSSTCs, (3) scatters in the strengths of SS materials, and (4) un-uniform distribution of low temperatures of SSSTCs during the testing.

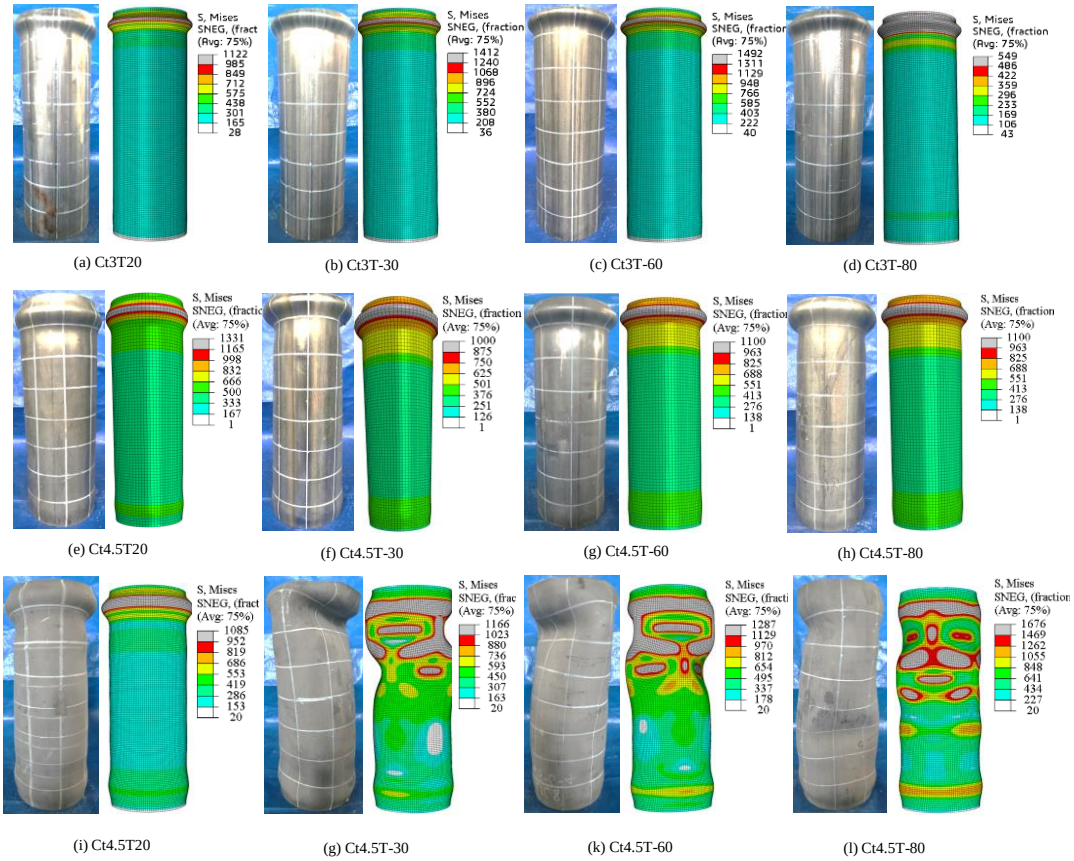

Fig. 18 Comparisons of failure modes between tests and FEM simulations

4.6. Conclusions

This paper firstly studied low-temperature compression behaviors of SSSTCs. Twenty SSSTCs with varying wall thickness were tested at different T levels. Including the tests, FEMs were also developed to simulate the low-temperature compression behaviors of SSSTCs. These experimental and numerical studies draw the following conclusions;

(1) Low temperatures improved the yield and ultimate strength, but reduced the ductility of SS 30408. As the T decreases from 20 to -30, -60, and -80℃, the average increments of yield (or ultimate) strength for SS in different thickness equal to 12% (27%), 25% (49%), and 29% (80%), respectively; meanwhile, the fracture strain of 3 (or 4.5, 6.0) mm-thick SS was reduced by 3% (16%, 6%), 2% (23%, 12%), and 11% (23%, 40%), respectively.

(2) Elephant foot local buckling occurred to most of the SSSTCs under low-

temperature compression. For specimens with t=6 mm thick SS tubes tested at -30~-80℃, inelastic inward and outward local buckling occurred.

(3) The low-temperature compression P-Δ curves of SSSTCs consist of four working stages, namely elastic, inelastic, plastic hardening, and recession stage. The length of the third-stage branch of P-Δ curves was determined by the D/t ratio of SS tube that determines the occurrence of local buckling in SS tube.

(4) The decreasing T increased the strength and stiffness of SSSTCs, but reduced their ductility. As the T decreases from 20 to -30, -60, and -80℃, the average increments in Pu of SSSTCs are 9%, 11%, and 18%, respectively; the average increments in K_0 of SSSTCs are 6%, 11%, and 15%, respectively; however, the Δ_u of SSSTCs was averagely reduced by 16%, 18%, and 9%, respectively.

(5) As t increases from 3.0 to 4.5 and 6 mm, the Pu values of SSSTCs tested at 20℃ (or -30, -60, -80℃) were increased by 73% (65%, 55%, 64%) and 127% (125%, 118%, and 136%), respectively; the K_0 values of SSSTCs tested at 20℃ (or -30, -60, -80℃) were increased by 70% (81%, 74%, 70%) and 140% (147%, 144%, and 129%), respectively; the Δ_u values of SSSTCs tested at 20℃ (or -30, -60, -80℃) were increased by 110% (91%, 106%, 97%) and 418% (402%, 453%, and 574%), respectively.

(6) The developed FEM reasonably predicted well compression behaviours of SSSTCs at low temperatures. The developed FEM offered average test-to-FE prediction ratios of 0.99, 0.99, and 1.05 for P_u, Δ_u and K_0, respectively.

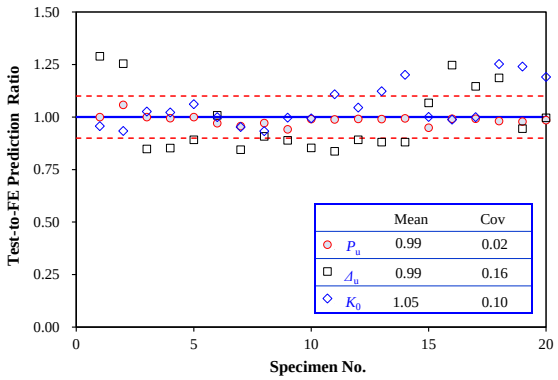

Fig. 19 Scatters of test-to-FE prediction ratios for P_u, Δ_u, and K_0

Nomenclature

A_s Cross-section area of SSSTC
DI Ductility ratio of SSSTC
D Diameter of SSSTC
E_{sT} Elastic modules of SSSTC tube at T
K_0 Initial stiffness of SSSTC
$K_{0,FE}$ Numerical initial stiffness
L Height of SSSTC
P_u Experimental ultimate compressive resistance
$P_{u,FE}$ Numerical ultimate compressive resistance
$P_{45\%}$ 45%P_u
T Low temperature
f_{yT} Yield strength at T
f_{uT} Ultimate strength at T
t Thickness of SSSTC
v_0 Initial imperfection amplitude of SSSTC
Δ_u Shortening of SSSTC at P_u
$\Delta_{u,FE}$ Shortening of SSSTC at $P_{u,FE}$
$\Delta_{45\%}$ Shortening of SSSTC at $P_{45\%}$
$\Delta_{85\%}$ Shortening at 85%P_u after peak load
σ_{ture} Ture stress
σ_{nom} Engineering stress
ε^{pl}_{ture} Inelastic true strain
ε_{nom} Engineering strain
ε_{yT} Yield strain at T
ε_{uT} Ultimate strain at T
ε_{FT} Fraction strain at T

Acknowledgment

The authors would like to acknowledge the financial supports by Municipal Education Commission of Tianjin Project（No.2019KJ122）, the Central University Fund Project (3122019106), and the Scientific Research Fund of Institute of Engineering Mechanics, China Earthquake Administration (Grant No. 2019EEEVL0504). The authors gratefully express their gratitude for the financial supports.

References

[1] Gardner L., “The use of stainless steel in structures”, Prog. Struct. Eng. Mater., 7 (2), 45-55, 2005.
[2] Burgan B., “Guidance on the use of stainless steel in construction, Structural applications of stainless steel in building and architecture”, Brussels, 2000.
[3] Buchanana Craig, Zhao Ou, Real Esther, Gardner L., “Cold-formed stainless steel CHS beam-columns-Testing, simulation and design”, Struct. Eng., 213, 110270, 2020.
[4] Gardner L., “Aesthetics, economics and design of stainless steel structures”, Adv. Steel Constr., 4(2), 113-122, 2008.
[5] Anwar U.H., Hani M.T., Nureddin M.A., “Failure of weld joints between carbon steel pipe and 304 stainless steel elbows”, Eng. Fail. Anal., 12, 181-191, 2015.
[6] Fissoloa A., Stelmaszykb J.M., Gourdin C., Bouin P., Pérez G., “Thermal fatigue loading for a type 304-L stainless steel used for pressure water reactor: investigations on the effect of a nearly perfect biaxial loading, and on the cumulative fatigue life”, Procedia Eng., 2, 15951604, 2010.
[7] Guan K., Wang Z.M., Gao M., Li X.Y., Zeng X.Y., “Effects of processing parameters on tensile properties of selective laser melted 304 stainless steel”, Mater. Des., 50, 581-586, 2013.
[8] Xie J., Cui N., Yan J.B., Yu J.H., “Experimental study on prestress losses of post-tensioned concrete members at ultra-low temperatures”. Struct. Concrete., 20, 1828-1841, 2019.
[9] Rasmussen K.J.R., “Full range stress–strain curves for stainless steel alloys”, J. Constr. Steel Res., 59, 47-61, 2003.
[10] Ashraf M., Gardner L., Nethercot D.A., “Strength enhancement of the corner regions of stainless steel cross-sections”, J. Constr. Steel Res., 61 (1), 37-52, 2005.
[11] Gardner L., Nethercot D.A., “Experiments on stainless steel hollow sections-Part 1: Material and cross-sectional behaviour”, J. Constr. Steel Res., 60 (9), 1291-1318, 2004.
[12] Quach W. M., Teng J. G., Chung K. F., “Three-Stage Full-Range Stress-Strain Model for Stainless Steels”, J. Struct. Eng., 134 (9), 1518-1527, 2008.
[13] Gardner L., Yun X., “Description of stress-strain curves for cold-formed steels”, Constr. Build. Mater., 189, 527-538, 2018.
[14] Sakumoto Y., Nakazato T., Matsuzaki A., “High-temperature properties of stainless steel for building structures”, J. Struct. Eng., 122 (4), 399-406, 1996.
[15] Chen J., Young B., “Stress–strain curves for stainless steel at elevated temperatures”, Eng. Struct., 28 (2), 229-239, 2006.
[16] Gardner L., Insausti A., Ng K.T., Ashraf M., “Elevated temperature material properties of stainless steel alloys”, J. Constr. Steel Res., 66 (5), 634-647, 2019.
[17] Wang X., Zhang J., DU Y., “High temperature mechanical properties of 00Cr17Ni14Mo2 stainless steel”, J. Build. Mater., 18 (5), 767-772, 2015.
[18] Liang Y., Manninen T., Zhao O., Walport F., Gardner L., “Elevated temperature material properties of a new high-chromium austenitic stainless steel”, J. Constr. Steel Res., 152, 261-273, 2019.
[19] Fan S.G., Jia L.L., Lyu X., Sun W.J., Chen M.H., Zheng J.C., “Experimental investigation of austenitic stainless steel material at elevated temperatures”, Constr. Build. Mater., 155, 267-285, 2017.
[20] Fan S.G., Ding R.M., Zheng J.C., Xie F.Z., Wu Q.X., “Refined Model for the Stress-Strain Curve of Austenitic Stainless-Steel Materials at Elevated Temperatures”, J. Mater. Civ. Eng., 32 (4), 04020032, 2020.
[21] Rasmussen KJR, “Recent research on stainless steel tubular structures”, J. Constr. Steel Res., 54 (1), 75-88, 2000.
[22] Young B., Hartono W., “Compression tests of stainless steel tubular members”, J. Struct. Eng.,128, 754-761, 2002.
[23] Lui W.M., Ashraf M., Young B., “Tests of cold-formed duplex stainless steel SHS beam-columns”, Eng. Struct., 74, 111-121, 2014.
[24] Huang Y., Young B., “Experimental investigation of cold-formed lean duplex stainless steel beam-columns”, Thin-Walled Struct., 76, 105-117, 2014.
[25] Arrayago I., Real E., Mirambell E., “Experimental study on ferritic stainless steel RHS and SHS beam-columns”, Thin-Walled Struct., 100, 93-104, 2016.
[26] Bu Y., Gardner L., “Laser-welded stainless steel I-section beam-columns: Testing, simulation and design”, Eng. Struct., 179, 23-36, 2019.
[27] Greiner R., Kettler M., “Interaction of bending and axial compression of stainless steel members”, J. Constr. Steel Res., 64 (11), 1217-1224, 2008.
[28] Zhao O., Gardner L., Young B., “Buckling of ferritic stainless steel members under combined axial compression and bending”, J. Constr. Steel Res., 117, 35–48, 2016.
[29] Cai Y., Young B., “Structural behaviour of cold-formed stainless steel bolted connections at post-fire condition”, J. Constr. Steel Res., 152, 213-321, 2019.
[30] Salih E.L., Gardner L., Nethercot D.A., “Numerical investigation of net section failure in stainless steel bolted connections”, J. Constr. Steel Res., 66 (12), 1455-1466, 2010.
[31] Elflah M., Theofanous M., Dirar S., Yuan H., “Behaviour of stainless steel beam-to-column joints — Part 1: experimental investigation”, J. Constr. Steel Res., 152, 183-193, 2019.
[32] GB/T 13239-2006, Metallic Materials – Tensile Testing at Low Temperature, China Standards Press, Beijing, 2006.
[33] Zhang R., Gardner L., Buchanan C., Matilainen VP., Piili H., Salminen A., “Testing and analysis of additively manufactured stainless steel CHS in compression”, Thin-Walled Struct., 159, 107270, 2021.
[34] Buchanan C., Matilainen V.P., Salminen A., Gardner L., “Structural performance of additive manufactured metallic material and cross-sections”, J. Constr. Steel Res., 136, 35-48, 2017.
[35] Yan J.B., Dong X., Zhu J., “Behaviours of stub steel tubular columns subjected to axial compression at low temperatures”, Constr. Build. Mater., 228, 116788, 2019.
[36] Guler S., Lale E., Aydogan M., “Behaviour of SFRC filled steel tube columns under axial load”, Adv. Steel Constr., 9(1), 14-25, 2013.
[37] Yan J.B., Luo Y.L., Su L., Lin X., Luo Y.B., Zhang L.X., “Low-temperature compression behaviour of square CFST columns using Q960 ultra-high strength steel”, Constr. Build. Mater., 183, 106727, 2021.
[38] Hibbitt H.D., Karlson B.I., Sorensen, EP (2009) ABAQUS/standard user’s manual, Version 6.14, 2014.
[39] Fan S.G., Li S., He B. B., Jia, L. L., Ding R. M., “Fire resistance performance analysis of high-strength steel Q550 columns under axial compression”, Adv. Steel Constr., 15(2), 185-191, 2019.
[40] Gardner L., Nethercot D.A., “Numerical modeling of stainless steel structural components-A consistent approach”, J. Struct. Eng., 130 (10), 1586-1601, 2004.